



Universiteit
Leiden
The Netherlands

Molecular dynamics study of the photodesorption of CO ice

Hemert, M.C. van; Takahashi, J.; Dishoeck, E.F. van

Citation

Hemert, M. C. van, Takahashi, J., & Dishoeck, E. F. van. (2015). Molecular dynamics study of the photodesorption of CO ice. *Journal Of Physical Chemistry A*, 119(24), 6354-6369.
doi:10.1021/acs.jpca.5b02611

Version: Publisher's Version

License: [Licensed under Article 25fa Copyright Act/Law \(Amendment Taverne\)](#)

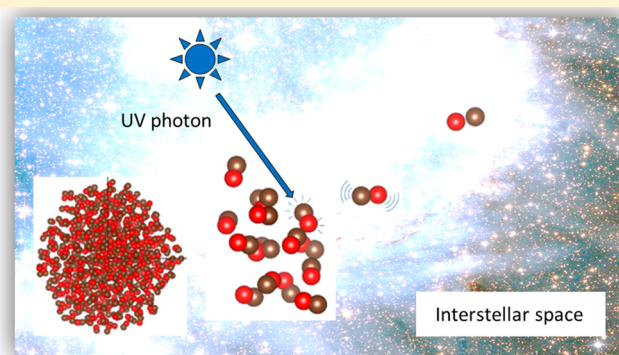
Downloaded from: <https://hdl.handle.net/1887/3197512>

Note: To cite this publication please use the final published version (if applicable).

Molecular Dynamics Study of the Photodesorption of CO Ice

Marc C. van Hemert,^{*,†} Junko Takahashi,[‡] and Ewine F. van Dishoeck[§][†]Leiden Institute of Chemistry, Gorlaeus Laboratories, Leiden University, Einsteinweg 55, 2333 CC Leiden, The Netherlands[‡]Faculty of Law, Meiji Gakuin University, 1518 Kamikurata-cho, Totsuka-ku, Yokohama 244-8539, Japan[§]Leiden Observatory, Leiden University, P.O. Box 9513, 2300 RA Leiden, The Netherlands

ABSTRACT: Photodesorption of CO ice is suggested to be the main process that maintains a measurable amount of gaseous CO in cold interstellar clouds. A classical molecular dynamics simulation is used to gain insight into the underlying mechanism. Site–site pair potentials were developed on the basis of *ab initio* calculations for the ground and excited nonrigid CO dimer. Both amorphous and crystalline CO clusters were created and characterized by their densities, expansion coefficients, binding energies, specific heats, and radial distribution functions. Selected CO molecules were electronically excited with 8.7–9.5 eV photons. CO returns to the ground state after a finite lifetime on the excited potential surface. Two desorption mechanisms are found: (1) direct desorption where excited CO is released from the cluster after landing on the ground state in an unfavorable orientation; (2) “kick-out” desorption where excited CO kicks out a neighboring CO molecule. These findings are in accord with laboratory experiments. Little dependence on size of the cluster, excitation energy and temperature in the 6–18 K range was found. The predicted photodesorption probability is 4.0×10^{-3} molecules photon⁻¹, smaller by a factor of 3–11 than that given by experiments.



1. INTRODUCTION

Carbon monoxide is an astrophysically important molecule. It is the second most abundant molecule observed in interstellar space after H₂ and the prime tracer of molecular gas. In solid form, it is also a key constituent to form more complex and prebiotic species.^{1–3} At the typical temperature in dense clouds, around 10 K, all molecules other than H₂ should stick onto dust grains and be kept as icy mantles on time scales shorter than the cloud lifetimes. Indeed, ices consisting of H₂O, CO, CO₂, and other minor species have been observed surrounding the grain cores in many dense clouds.^{4,5} The solid cores onto which the ices are adsorbed are made of silicates or carbonaceous material with a diameter of typically 0.1 μm (see, e.g., refs 6 and 7). The ices are often found to be layered, with pure CO ice on top of a water-rich ice layer, based on the shapes of the strong CO ice absorption bands (see, e.g., refs 8–10).

At densities above 10⁵ particles cm⁻³, all molecules including CO are predicted to be frozen out as ice. Surprisingly, a measurable amount of gaseous CO is detected in cold regions where thermal desorption is negligible (see, e.g., refs 11–13). Nonthermal desorption can occur by photon-induced and cosmic-ray-induced processes. Even in dense clouds, external UV photons from the interstellar radiation field can penetrate into its outer regions. Cosmic rays are present throughout interstellar space, and create additional UV photons deep inside clouds through interaction with H₂.¹⁴ Thus, photodesorption of CO ice has been suggested as a possible mechanism to keep a small abundance of gaseous CO in the regions with UV

photons (see, e.g., refs 15–17). An accurate determination of the probability of this process and a good understanding of the mechanism by which this takes place is therefore warranted.

In the laboratory, photodesorption of interstellar CO ice has been simulated under ultrahigh vacuum conditions and at astrophysically relevant temperatures by Öberg et al.,^{17–19} Muñoz Caro et al.,²⁰ Fayolle et al.,²¹ Chen et al.,²² and Cruz-Díaz et al.²³ CO ice films were prepared by depositing CO molecules on a gold substrate cooled down to 7–18 K and the photodesorption process of CO ice during irradiation using a hydrogen (D₂) discharge lamp was monitored by reflection absorption infrared spectroscopy (RAIRS) and quadrupole mass spectroscopy (QMS). The D₂ discharge lamp covers the UV energy of 7–10.5 eV, often with a strong peak at 10.2 eV corresponding to Lyman α. The thickness of the deposited ice in monolayers (ML) was monitored in an isothermal experiment with RAIRS. The thickness of CO thin ice films prepared by Öberg et al.,^{18,19} Muñoz Caro et al.,²⁰ and Fayolle et al.²¹ were 3.5–4, 12–16, and 9–10 monolayers (ML), respectively.

The values of photodesorption probabilities per incident photon derived by Öberg et al.^{18,19} and Muñoz Caro et al.²⁰ are 2.7×10^{-3} and $(3.5–6.4) \times 10^{-2}$ molecules photon⁻¹, respectively. These numbers are orders of magnitude higher

Received: March 18, 2015

Revised: May 23, 2015

Published: May 26, 2015



than the value that was originally estimated by Greenberg²⁴ and had been used in previous astrochemical networks. There is also a difference by a factor of 13–24 between the values derived by these groups. Fayolle et al.²¹ suggested that this discrepancy could originate from different flux ratios produced by the laboratory lamps across the spectral window and therefore studied the wavelength dependence of the photodesorption of CO ice. Consistent with the suggestion by Öberg et al.,¹⁷ they found that the desorption spectrum exactly follows the CO VUV absorption spectrum into the first excited electronic state, and that the absorption is close to zero at Lyman α . They therefore labeled the desorption process as a DIET (desorption induced by electronic transition) process.

In interstellar clouds, the freeze-out process occurs very slowly at low densities, on a one by one molecule basis, so the structure of the resulting CO ice mantle should be amorphous. But, it has also been suggested that a large fraction of pure interstellar CO ice could be crystalline, because migration of CO molecules and rearrangement of the structure of CO ice can occur in star-forming clouds at temperatures just below the CO desorption temperature.²⁵ Thus, we consider both amorphous and crystalline CO clusters as the models for the interstellar CO ice.

To study the mechanism of the photodesorption process of CO ice and estimate the photodesorption probabilities theoretically, we performed a classical molecular dynamics (MD) simulation of CO ice. For our MD simulation, we calculated *ab initio* 4-dimensional potential energy surfaces for a pair of interacting CO molecules with a number of intramolecular distances both for the electronic ground state and for the first electronic excited state. On the basis of the *ab initio* results, we developed the site–site potential energy functions for the ground- and excited-state nonrigid CO dimer, because the vibrational motions and the electronic excited states play important roles for the photodesorption process. We generated amorphous and crystalline CO clusters, excited one of the CO molecules with an energy corresponding to an 8.7–9.5 eV UV photon, and monitored the MD trajectories that lead to CO desorption.

In our model for photodesorption, we assume that the excited CO molecule stays in the first electronic excited state for a finite, subpicosecond, time. During that time lapse the motion of the excited molecule and the surrounding molecules are determined by the interaction force field for the excited molecule. The excited molecule and the surrounding molecules then find their new equilibrium geometries. We assume that at the end of that time lapse the excited molecule undergoes internal conversion to the electronic ground state (because UV fluorescence is comparatively slow) and then the motion is again dictated by the ground-state interaction potential. It may then happen that on the ground-state potential energy surface the excited molecule is no longer in a bound configuration and then desorption of the molecule is observed during this final motion. Because CO has a dissociation energy above 11 eV, no fragmentation into energetic C and O atoms will occur in the photodesorption process of CO ice studied here. Our model differs in this respect from the model used in the MD simulations that was performed to explain the observed photodesorption of H₂O ice.^{26–28} In that process, the H₂O molecule first dissociates into an H atom and an OH radical that share 1–3 eV of excess dissociation energy, because the first electronic excited state is repulsive. These fragments can

then directly desorb, recombine, and/or kick out neighboring molecules.

Our model is in accord with the following conclusions (a) and (b) reached in the pioneering CO photodesorption modeling by Galloway and Herbst²⁹ and Dzegilenko and Herbst,³⁰ respectively. (a) Vibrational excitation only of a CO molecule adsorbed onto a surface (e.g., by IR radiation) hardly leads to desorption. (b) For desorption to occur, it needs induction to a librational type motion, e.g., induced by excitation of a neighbor molecule of different chemical nature. In our model, this librational motion is induced by the differences in anisotropy of ground and excited-state interaction potentials.

In section 2, we present the computational details for obtaining the potential energy functions and performing MD simulations. In section 3, we present results and discussion. In section 4, the results are summarized and some concluding remarks are given.

2. METHOD

2.1. *Ab Initio* Potential Energy Surface for the Ground-State CO Dimer. Many spectroscopic studies have been performed of the CO dimer (see, e.g., refs 31–33). Some *ab initio* potential energy surfaces have been calculated to study spectroscopic properties of the CO dimer.^{34,35} The most accurate *ab initio* 4-dimensional potential energy surface at the time of the start of our research was calculated by Vissers et al.³⁶ for the CO dimer consisting of rigid CO molecules to study its rovibrational spectrum. They used the CCSD(T) method with a standard aug-cc-pVTZ basis set augmented with bond functions centered at the midpoint between the two CO molecules. A newer and slightly more accurate surface has since been calculated by Dawes et al.³⁷ We first calculated the interaction potential energy surface still following upon the work by Vissers et al.³⁶ for the rigid CO dimer using the aug-cc-pVQZ basis set without the bond functions instead. Then, we developed the potential energy surface into those for the nonrigid CO dimer not only in the ground state but also in the excited state, because the vibrational motions and the electronic excited states play important roles in the photodesorption process. We choose a dimer approach because of the required detail of the potential in the subsequent dynamics. Detail in dependence on orientation, inter- and intramolecular distances, and electronic excitation that would be impossible to reach in a cluster or surface approach without loss of reliability because of computer time constraints.

The potential energy surface for the ground-state nonrigid CO dimer was developed originally for the study of the photodesorption process of CO ice. It has also been used also in the study of the dynamics of CO molecules adsorbed on the surface of amorphous water ice and was described there in some detail.³⁸ Here, we briefly summarize.

The *ab initio* 4-dimensional potential energy surfaces were calculated for the CO dimer for three CO bond distances, i.e., that of molecule A, $r_{\text{CO}}(\text{A})$, was kept at the ground-state equilibrium value $r_e = 2.132$ bohr, whereas that of molecule B, $r_{\text{CO}}(\text{B})$, had three values, r_e , $r_e + 0.1r_e$, and $r_e - 0.1r_e$. Each 4D grid consisted of 7 θ_A angles, 7 θ_B angles, 6 φ angles and 12 R values (3.5, 3.75, 4.0, 4.25, 4.5, 5.0, 5.5, 6.0, 6.5, 7.0, 9.0, 20.0 Å). The geometry conventions are shown in Figure 1. The angles were chosen to enable a spherical expansion of the interaction energy. The total number of terms in the expansion was 140 corresponding to a maximum value of $L = 6$ in the

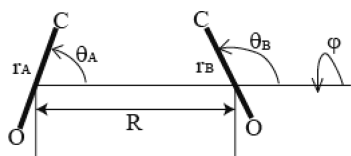


Figure 1. Coordinate system of the CO dimer.

associated Legendre polynomials in the angular basis functions. The interaction energy was found from CCSD(T) calculations using a standard aug-cc-pVQZ basis set. The Boys–Bernardi counterpoise correction³⁹ was applied:

$$E_{\text{int}}(r_A, r_B, R, \theta_A, \theta_B, \varphi) = E_{\text{CCSD}}(r_A, r_B, R, \theta_A, \theta_B, \varphi) - E_{\text{CCSD}}(\text{A})(r_A, r_B, R, \theta_A, \theta_B, \varphi) - E_{\text{CCSD}}(\text{B})(r_A, r_B, R, \theta_A, \theta_B, \varphi) \quad (1)$$

where E_{CCSD} , $E_{\text{CCSD}}(\text{A})$, and $E_{\text{CCSD}}(\text{B})$ are the energies for the CO dimer at the specified geometry, of molecule A in the full dimer basis set at the specified geometry, and of molecule B in the full dimer basis set, respectively. All calculations were performed with the MOLPRO program.⁴⁰

To express the potential explicitly in terms of radial and angular variables, we used the spherical expansion method.^{41,42} For the CO dimer system, 6 L_a , 6 L_b , and 12 L values were included to generate 140 expansion coefficients in total at each of the 12 R values and at each of the three $r_{\text{CO}}(\text{B})$ values. At

each $r_{\text{CO}}(\text{B})$, a cubic spline fit was made for each $L_a L_b L$ as a function of R . This fit was then used to generate contour plots of the potential.

In Figure 2, the contour plots for the *ab initio* potential energy surface for the ground-state CO dimer are given. It is seen that there are two minima separated by a barrier. The lowest minimum occurs with an interaction energy of 128 cm^{-1} for the geometry where the two CO molecules are parallel with $\theta_A = 45^\circ$ and $\theta_B = 135^\circ$ and thus the two oxygen atoms are the closest together. The other minimum is found at 118 cm^{-1} for $\theta_A = 120^\circ$ and $\theta_B = 60^\circ$ with the two carbon atoms the closest together. The accuracy of the energies recalculated from the spline interpolated spherical expansion coefficients is better than 0.5 cm^{-1} in the region of the minima. The energies for the minima are somewhat smaller (in absolute sense) than the values obtained by Visser et al.,³⁶ presumably due to the absence of the bond functions in our calculations. The center of mass distances for the minima are 4.3 and 3.7 Å, respectively.

2.2. Site–Site Potential Energy Function for the Ground-State CO Dimer. For MD simulations, the spherical expansion parametrization is too expensive. Instead, the *ab initio* interaction potential was parametrized as a site–site potential with electrostatic, exchange repulsion, and dispersion contributions plus Morse potentials:

$$V = V_{\text{elst}} + V_{\text{exch}} + V_{\text{disp}} + V_{\text{Morse,A}} + V_{\text{Morse,B}} \quad (2)$$

The electrostatic part is expressed as

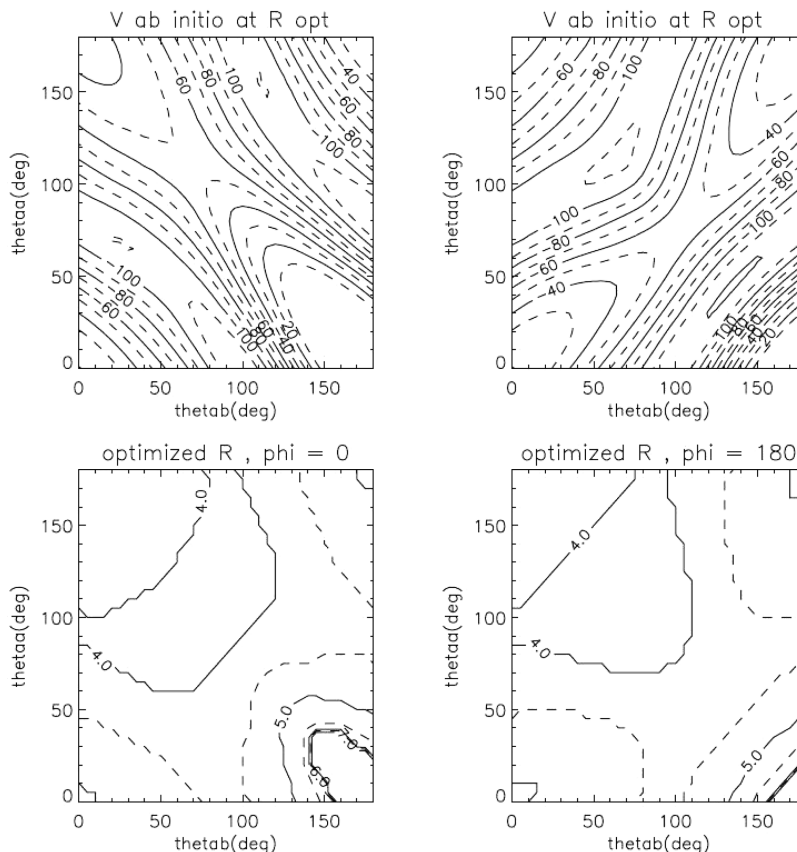


Figure 2. Contour plots for the *ab initio* potential energy surface for the ground-state CO dimer. Upper panels: Contour plots of the potential energy for θ_A and θ_B at $\varphi = 0^\circ$ (left) and $\varphi = 180^\circ$ (right), respectively, at the equilibrium CO bond distances, where the intermolecular distance R is optimized at each θ_A and θ_B value. Lower panels: Contour plots of the optimized intermolecular distance R for θ_A and θ_B at $\varphi = 0^\circ$ and $\varphi = 180^\circ$, respectively.

$$V_{\text{elst}} = \sum_{i \in A} \sum_{j \in B} \frac{Q_i Q_j}{r_{ij}} \quad (3)$$

where r_{ij} is the distance between the two charge sites. The charges Q_i and Q_j are located on the atoms and on the molecular centers of mass. The resulting forces on the mass-less centers of mass are distributed into forces on the atoms in such a way that total force is conserved and no torque is introduced. The values of the charges are initially chosen to exactly reproduce the dipole and quadrupole moments at the specific intramolecular distance r_{CO} . The moments were taken from MCSCF/CCI calculations with the AVQZ basis. The exchange repulsion part is expressed as

$$V_{\text{exch}} = \sum_{i \in A} \sum_{j \in B} A_{ij} \exp(-B_{ij} r_{ij}) \quad (4)$$

and the dispersion part as

$$V_{\text{disp}} = \sum_{i \in A} \sum_{j \in B} \frac{C_{ij}}{r_{ij}^6} \quad (5)$$

The parameters A_{ij} and C_{ij} were optimized by the least-squares procedure where all interaction energies with values below 200 cm^{-1} were included. The criterion of 200 cm^{-1} was chosen to focus the optimization of the potential on the bound area. The values of the parameters B_{ij} were initially derived from the relation between the standard Lennard-Jones C_6 and C_{12} coefficients and the parameters used here, as given by Lim.⁴³ The parameters B_{ij} and the charges were then slightly adapted to minimize the least-squares standard deviation. It was found that the interaction energy could be well represented when only the electrostatic term was made dependent on the CO bond distance. More specifically, the changes in the charges were made proportional to the changes in the computed charges derived from the *ab initio* dipole and quadrupole moments as

$$Q_i = Q_i^0 \exp\{-\alpha_i(r_{\text{CO}} - r_e)\} \quad (6)$$

The standard Morse potential is expressed as

$$V_{\text{Morse}} = D_e [1 - \exp\{-\beta(r_{\text{CO}} - r_e)\}]^2 \quad (7)$$

The Morse parameters for the CO monomer, D_e and β , were found from a fit to the experimental data. The resulting values of the fit parameters appearing in eqs 3–7 for the electronic ground-state CO dimer are given in Table 1.

In Figure 3, the contour plots based on the fit parameters are given for the interaction energies and for the associated center of mass distances. Given the simple form of the parametrized potential, the agreement between the full *ab initio* contours and the model contours is satisfying. In the fitted potential the global minimum is correctly reproduced, both in well depth and in orientation, and also the barrier toward a secondary minimum is reproduced fairly well; however, there the mutual orientation of the molecules is slightly different from the *ab initio* result. The model molecules are somewhat softer than the *ab initio* ones. This is in part due to the bias in the selection of configurations used in the least-squares fit. Nevertheless, the use of these fit parameters in MD simulations does not lead to large differences between calculated and experimental densities for the CO cluster with α -phase crystalline structure (section 3.1).

2.3. *Ab Initio* Potential Energy Surface for the Excited-State CO Dimer. The first electronic excited state of CO is the

Table 1. Values of the Parameters (atomic units) That Are Included in the Site–Site Potential Energy Functions (Eqs 3–7) for the Ground-State and the Excited-State CO Dimer

parameter	ground state	excited state
$r_{e,A}$	2.132	2.132
$r_{e,B}$	2.132	2.334
A_{CC}	13.28	11.30
A_{OO}	234.1	216.9
A_{CO}	55.74	81.40
A_{OC}	55.74	106.0
B_{CC}	1.50	1.50
B_{OO}	2.250	2.250
B_{CO}	1.875	1.875
B_{OC}	1.875	1.875
C_{CC}	−55.98	−30.80
C_{OO}	−17.65	−6.36
C_{CO}	−25.42	−41.50
C_{OC}	−25.42	−51.10
Q_C^0	−0.470	−0.8
Q_O^0	−0.615	−0.7
α_C	2.034	0.0
α_O	1.128	0.0
β	1.232	1.623
D_e	0.4127	0.1165

A $^1\Pi$ state (see, e.g., refs 44 and 45). When a CO molecule in this excited state is approached by another CO molecule in the electronic ground state, the cylindrical symmetry of the excited CO is lost and the degenerate Π state will split in two. When a plane of symmetry still remains, the group is C_v , and the two states will belong to A' and A'' irreducible representations and should again become degenerate at large intermolecular distance. Because the CCSD method that we used for the calculation of the ground-state interaction energy cannot be used for singlet excited states, various other options for the calculation of the interaction energy between an excited-state CO molecule and a ground-state CO molecule have been tested.

First, the calculation of the interaction energy between a CO molecule in a triplet Π excited state and a CO molecule in the electronic ground state was studied using the RCCSD(T) formalism under the assumption that the interaction potential for singlet and triplet would not differ too much. To avoid ambiguity on which of the two molecules becomes excited, the molecule to be excited was given a larger bond length. This should work well because both the A $^3\Pi$ and A $^1\Pi$ state have an equilibrium bond length about 10% longer than that of the ground state. Again the counterpoise method was applied and the same atomic orbital basis set was used. The triplet reference determinant was found from an RHF calculation for the lowest triplet state. It was verified in the RHF calculation that the excitation was indeed of the molecule with the longest bond length. The calculations were performed for 12 R values (3.5, 3.75, 4.0, 4.25, 4.5, 5.0, 5.5, 6.0, 6.5, 7.0, 9.0, 12.0 Å), 2 φ values (0° and 180° , such that always a plane of symmetry is present), three ground-state molecular orientations (0° , 90° , 180°), and five excited-state orientations (0° , 45° , 90° , 135° , 180°).

In practice, this approach did not work to satisfaction. It turned out that there exists a metastable molecule OCCO in the triplet ground state with its energy only 3 eV above that of CO–CO in the singlet ground state. Especially the $^3A''$ state had low energies even when the CO–CO* complex had a

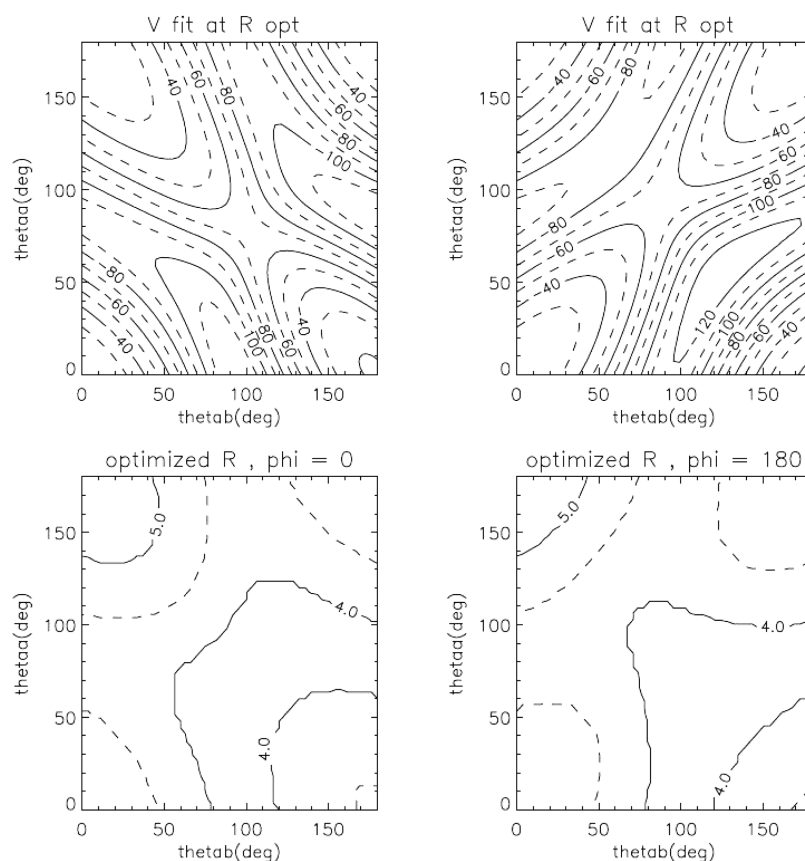


Figure 3. Contour plots for the site–site potential energy function for the ground-state CO dimer. The site–site potential energy function is described as eqs 2–7 and the values of the parameters in this function are taken from Table 1. See the captions in Figure 2 about the upper and lower panels.

geometry rather remote from the OCCO equilibrium (see, e.g., ref 46). So, in retrospect, this was not a good choice. Therefore, subsequent calculations used the MRCI method directly for the singlet excited states, although this method has the drawback that it is not size consistent and has no possibility for counterpoise corrections. Because it was found to be impossible to obtain converged CI results with one and the same set of control parameters, and without the use of symmetry, all calculations were ultimately done in C_s symmetry, implying that the two CO molecules lie in a plane.

The CI procedure was as follows: first a closed shell SCF for the CO dimer was performed, then an MCSCF calculation with the 8 core electrons in 4 frozen SCF orbitals of a' symmetry, another 8 electrons in 4 doubly occupied, but still to be optimized, a' orbitals and the remaining 12 active electrons in 6 a' and 4 a'' orbitals. The state-averaged calculations were performed for three singlet A' states and two singlet A'' states. In the subsequent contracted CI calculations, three $^1A'$, two $^1A''$, two $^3A'$, and two $^3A''$ states were obtained. The second singlet A' -state energies and the first singlet A'' -state energies were used together in the fit procedure, implying that an averaged potential was used for the excited-state CO dimer in MD simulations.

2.4. Site–Site Potential Energy Function for the Excited-State CO Dimer. Because all of the 600 geometries had a plane of symmetry and only a limited number of orientations were considered, no spherical expansion could be performed. The fit of the excited-state potential energy surface to the site–site potential energy functions was performed along

the same lines as described above for the ground state. The same B_{ij} parameters were used as in the ground state. The charges were initially set at the values derived from the *ab initio* MRCI dipole and quadrupole moments of the monomer in the $A\ ^1\Pi$ state and later slightly adjusted for the optimal standard deviation of the least-squares fit. The geometries related to the formation of the OCCO molecule, so with short C–C distances, and the geometries with their energies above 400 cm^{-1} , were excluded from the fit.

The resulting values of the fit parameters for the excited-state CO dimer are given in Table 1. The standard deviation of the excited-state fit is 10 cm^{-1} , which is similar to that of the ground state. Contour plots for the fitted excited-state potential are given in Figure 4. Compared with the ground-state potential, it is obvious that the excited CO molecule prefers a different orientation with respect to its neighbor. The optimal intermolecular distances are rather similar for ground and excited molecule interaction.

2.5. Preparation of CO Clusters. In our MD simulations, we adopted two types of CO clusters as models of pieces of interstellar CO ice, amorphous and crystalline ones, each consisting of limited numbers of CO molecules. Those clusters were created by starting from the initial geometries given by the different methods as described in the following.

A series of amorphous clusters consisting of 200, 300, 500, 800, and 1200 CO molecules were created. Their initial geometries were generated by adding CO molecules, one by one, to previous CO molecules. The two polar angles defining the orientation of the vector connecting the cluster center of

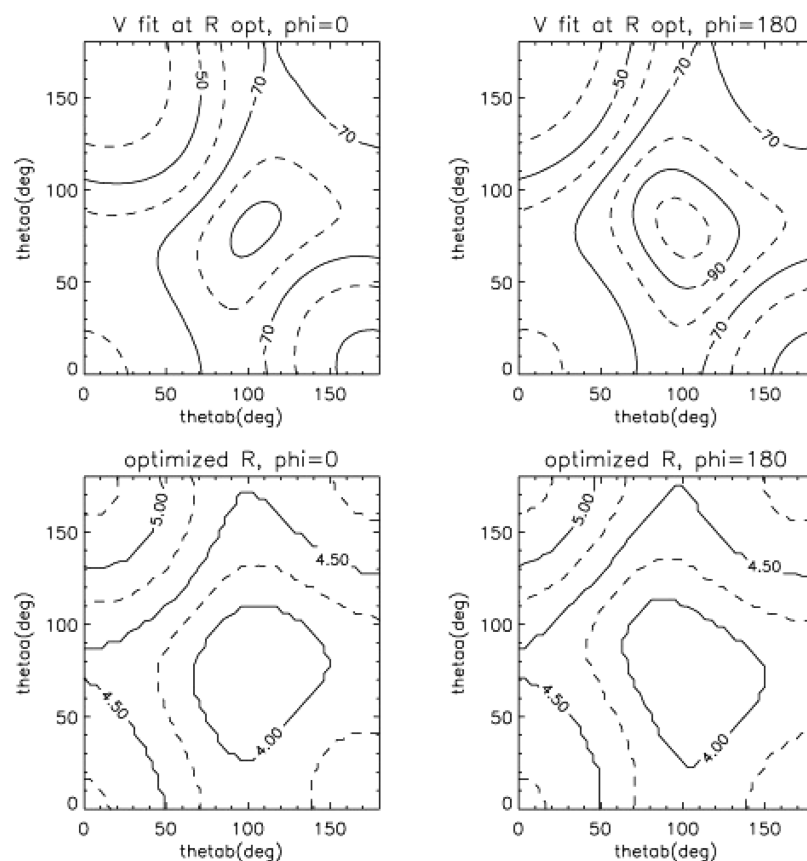


Figure 4. Contour plots for the site–site potential energy function for the excited-state CO dimer. In this CO dimer, molecule A is in the ground state and molecule B is in the excited state. See the captions in Figure 2 about the upper and lower panels. The equilibrium CO bond distances of molecule A and B are those for the ground and excited state, respectively.

mass to the center of mass of the new molecule and the two polar angles defining the orientation of the internuclear axis of the new molecule were determined by a random number generator. The new molecule was set at 10 Å from the surface of the core formed by the molecules already present. The energetically most favored final position of the new molecule was then determined with the simplex method.⁴⁷ The positions of the molecules already present were kept frozen. The energies in the simplex procedure were derived from the fitted ground-state potential energy surface. For each size of amorphous CO cluster, we made five different samples by using different starting parameters for the orientations in the grow procedure.

Also a series of CO clusters were created with a close to the cubic α P2₁3 phase crystalline structure. First, a $8 \times 8 \times 8$ unit cell cluster was constructed using the standard crystal data⁴⁸ as input. Then, cuts were made to generate spherical clusters containing 221, 522, and 1055 CO molecules.

2.6. Molecular Dynamics Simulation of CO Clusters.

The classical MD simulations were performed using the velocity Verlet scheme⁴⁹ for time propagation. The forces were calculated analytically from the site–site potential energy functions given in eqs 2–7.

At the first stage of our simulations, the samples of CO clusters prepared in section 2.5 were made to undergo temperature cycling in an MD procedure, in 6 K steps from 0 to 30 K and back to 6 K, using the ground-state potential energy functions for the CO systems. The time step was 20 au (~ 0.5 fs) and the duration was 10 000 steps at each temperature. The clusters were thus kept for 200 000 au of

time (~ 5 ps) at each temperature, and the total simulation time was ~ 50 ps. Temperatures were regulated with a Berendsen thermostat⁵⁰ with 4000 au time constant. Properties of the CO clusters obtained here were examined. The results are shown and discussed in section 3.1.

At the second stage of our simulations, each sample cluster was reheated to 6 K from the coordinates obtained in the temperature cycling procedure, where the time step was 20 au (~ 0.5 fs) and the duration was 5000 steps. The total time of the warm-up period was thus 2.5 ps. After re-equilibration, the thermostat was switched off and absorption of a UV photon was simulated by bringing a selected CO molecule vertically, with conservation of internuclear distance, into an excited state and adapting the nuclear momenta to the excited-state vibrational energy. For the dynamics on the excited-state potential energy surface, the time step was 4 au (~ 0.1 fs) and the duration was 1000 steps plus a random number between 0 and another 5000 steps. The total time in the excited state was thus between 0.1 and 0.6 ps. This scheme and the particular time interval were chosen on the basis of arguments presented in section 3.2. It is assumed that after the time in the excited state the molecule returns to the ground state by a process of internal conversion. This process was simulated by adapting again only the nuclear momenta of the atoms and letting the motions continue high up on the ground-state potential energy surface. During another 50 000 steps with a time step of 4 au, the positions of the CO molecules were monitored. The total time of the period after the internal conversion was thus ~ 5 ps. Photodesorption was defined as having occurred when the CO

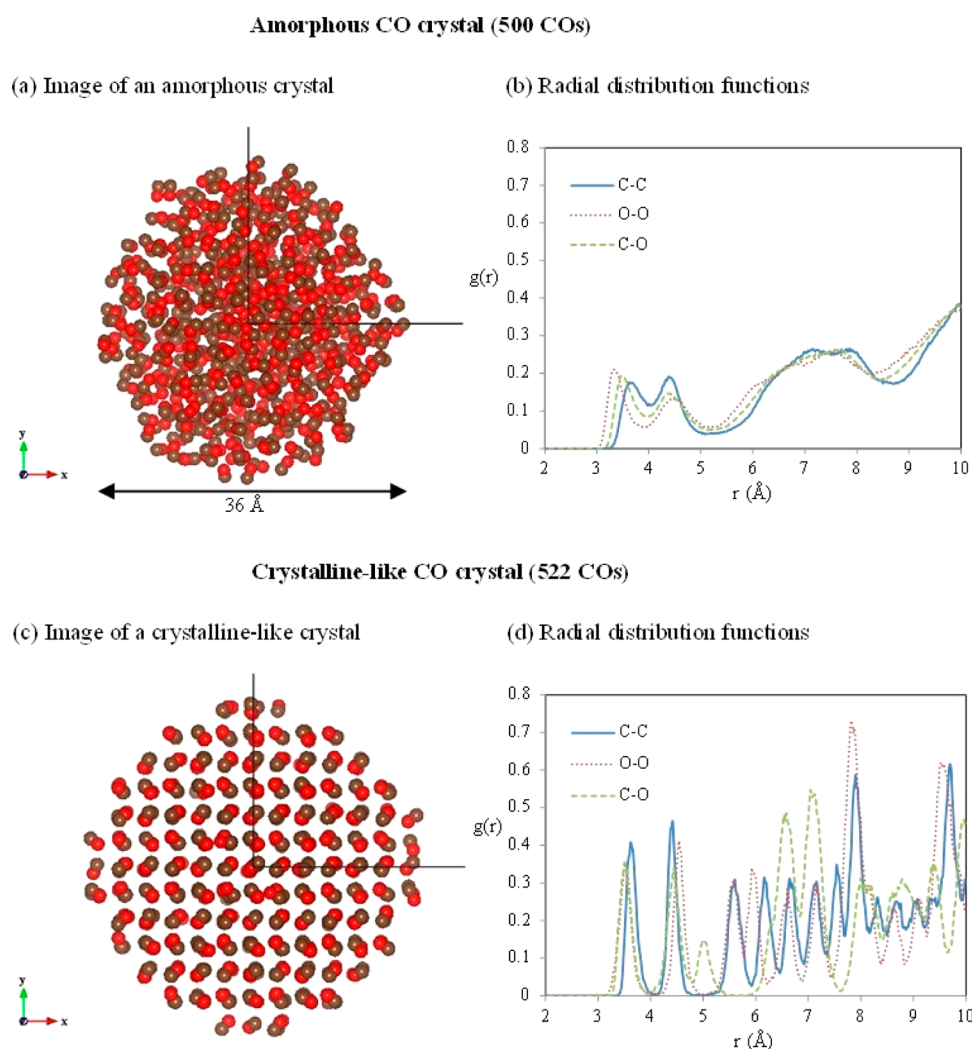


Figure 5. (a) Image of an amorphous sample cluster with 500 CO molecules after 50 ps temperature cycling in an MD procedure at 6 K. (b) Radial distribution functions for (a), in arbitrary units. (c) Image of a crystalline sample cluster with 522 CO molecules after 50 ps temperature cycling in an MD procedure at 6 K. (d) Radial distribution functions for (c), in arbitrary units.

molecule was more than 6 Bohr removed from the surface layer of the sample clusters and its binding energy to the remaining cluster was less than its translational energy. The results are shown and discussed in section 3.3.

For each sample cluster, only one CO molecule at the time was excited and only a fraction (between 0.2 and 1, see sections 3.3–3.5 for details) of the CO molecules in the cluster was selected for excitation. The excitation energies, 8.7, 9.1, and 9.5 eV, were used to investigate the wavelength dependence. Excitation energies below 8.6 eV are not accessible in our simulations, because in those cases the vertical excitation out of the CO geometries sampled at 6 K ends in the classically forbidden region of the excited-state potential. The effect of the temperature of CO clusters was also studied by raising the temperature in the re-equilibration phase to 12, 18, or 24 K instead of 6 K.

3. RESULTS AND DISCUSSION

3.1. Properties of CO Clusters. For the evaluation of the quality of the ground-state potential energy surface used in our simulations, we have two sets of key reference data: first, the structure of the clusters as manifest through the radial distribution functions and the density, and second the lattice

energy and the specific heat. We examined these properties of the CO clusters that were obtained at the first stage of our simulations.

The CO clusters whose initial geometries were determined by the simplex method shrink more and more during the initial 10 ps temperature cycling in an MD procedure, because they have loose structures. After 20 ps, we find no more significant change in their structures. After this cycling, the O–O, C–C, and C–O radial distribution functions of these clusters show a broad but still very well discernible structure. Clearly, the CO clusters are rather amorphous. The average radii of the resulting amorphous clusters containing 200, 300, 500, 800, and 1200 CO molecules are 14.0, 16.0, 18.0, 21.0, and 24.5 Å, respectively.

Heating the CO clusters with the cubic α $P2_13$ phase crystalline structures by 20 ps temperature cycling in an MD procedure shows the gradual transition to more liquid like states (experimentally observed as melting). However, they keep crystalline structures even after 50 ps, which is different from the CO clusters starting from amorphous structures. This is because an amorphous structure itself is one of the many local minima in the potential energy surface and the transition barrier out of a crystalline structure into a more irregular

Table 2. Average Binding Energies per Molecule for the Sample CO Clusters of Various Sizes and Temperatures

cluster-type	no. of CO molecules in cluster	average binding energies per molecule (cm^{-1})			
		6 K	12 K	18 K	24 K
amorphous	200	507 \pm 2			
	300	529 \pm 2			
	500	550 \pm 1			
	800	575 \pm 1	553 \pm 1	528 \pm 1	502 \pm 1
	1200	598 \pm 1	566 \pm 1	542 \pm 1	517 \pm 1
crystalline	221	542			
	522	589			
	1055	625	603		

structure is higher than the energy available at those temperatures. The radial distribution functions for the crystalline CO clusters are much sharper and also reflect a slightly higher density. For the crystalline clusters containing 221, 522, and 1055 CO molecules, the radii are 13.0, 17.5, and 22.5 Å, respectively.

The structure of the various clusters becomes clearest when looking at the radial distribution functions. Because the radial distribution functions vary little for the various sizes, we give only two specific examples in Figure 5: an amorphous cluster containing 500 CO molecules and a crystalline one containing 522 CO molecules. In both cases, the sample clusters are obtained after 50 ps temperature cycling in an MD procedure at 6 K. The radial distribution functions are obtained by averaging over 250 and 522 time steps for the amorphous and crystalline samples, respectively.

In the amorphous CO clusters, the first peak for the C–C distance is at 3.66 Å and the fwhm is 0.40 Å, for O–O the peak is at 3.32 Å and the width 0.36 Å, and for C–O the peak is at 3.50 Å and the width 0.45 Å. The values hardly vary not only for the different samples of the same size but also for the samples containing different numbers of CO molecules. In the crystalline CO clusters, the first peaks are at 3.63, 3.52, and 3.50 Å and the FWHMs are 0.22, 0.25, and 0.28 Å for C–C, O–O, and C–O, respectively. Most notable is the relatively short nearest neighbor O–O distance in the amorphous CO clusters when compared with the crystalline ones.

No experimental data seem to be available for the radial distribution functions of amorphous CO clusters. There are several reference data by theoretical studies. Lattice dynamics calculations based on an *ab initio* potential for crystalline α -CO by Janssen et al.⁵¹ show that initially the C–C distance is shortest, but that after temperature cycling the O–O distance becomes the shortest. The potential energy surface calculated by Vissers et al.⁵² shows two minima at slipped antiparallel structures: the global minimum with the C–C distance smaller than the O–O distance and a local minimum where the O atoms are closer together. The temperature cycling thus nicely restores the ordering of the CO to the proper one.

The density of the crystalline samples containing 1055 CO molecules was calculated as 1.05 g/cm³ at 6 K. This value compares well with the density of 1.03 g/cm³ derived from the X-ray based fcc unit cell length of 5.64 Å.⁵³ The density of the amorphous samples is about 2% lower than that of the crystalline samples. We derived a volumetric expansion coefficient of $\sim 2.0 \times 10^{-3}/\text{deg}$ from the temperature dependence of the density of the various clusters. It is hard to compare this value with any experimental values (see, e.g., ref 53), because in reality the CO clusters behave in this respect more like Einstein crystals than classical crystals. Our expansion

coefficient corresponds to the value at 50 K in the reference mentioned above.

In Table 2, the average energies per molecule (in cm^{-1}) are summarized for the sample CO clusters of various sizes and temperatures. From these numbers, we can derive the specific heat of the cluster and make an estimate of the binding energy that would be obtained for an infinite crystal. The average specific heat corresponds to 4 cm^{-1}/K equivalent to 6 R, exactly what one would expect from a classical system with 6 degrees of freedom (3 for translation, 2 for rotation, and 1 for vibration). Yet, we find that the vibration hardly contributes to the kinetic energy at the temperatures considered here. Further, we notice that by raising the temperature the increase in total kinetic energy is not accompanied by an equal increase in the potential energy. Such an equality (actually the equipartition principle) is only valid for the systems under the influence of harmonic forces.

Of course, one cannot compare our calculated specific heats with experimental values (see, e.g., ref 53), because we completely neglect the quantum effects that would dominate at the low temperatures considered here. The calculated lowest phonon frequency corresponding to a coupled rotational-translational motion is $\sim 40 \text{ cm}^{-1}$, equivalent to 60 K, such that the classical limit of an Einstein crystal is not reached for our temperature range. Extrapolation of the amorphous cluster data leads to an estimated value of $\sim 625 \text{ cm}^{-1}$ for an infinite amorphous crystal at 6 K. Adding 25 cm^{-1} as an estimated difference between an amorphous sample and a crystalline one and an additional 25 cm^{-1} for extrapolation to 0 K would bring the estimated lattice energy of an infinite crystal to 675 cm^{-1} , which is very close to the experimental value of 690 cm^{-1} .

3.2. Mechanism of CO Photodesorption. In our simulations, we have aimed to be consistent with the knowledge of the absorption spectrum of solid CO. The width of the vibrational bands observed in the VUV absorption spectrum of solid CO in the 7.9–9.5 eV region is 500 cm^{-1} .^{23,54,55} The orders-of-magnitude larger than gas-phase line width could have three different origins: (i) Pure lifetime broadening, which would imply that the excited state would convert to another state within 5 fs. (ii) Inhomogeneity of the sample, i.e., each CO molecule would require somewhat different excitation energy to end up in a particular vibrational level. (iii) There is an exciton mechanism, not a single molecule is excited but a whole set, and what is observed is an exciton band.⁵⁶

It is known that for solid CO diluted in an argon matrix the vibrational line width in the VUV absorption spectrum is still very large, $\sim 250 \text{ cm}^{-1}$.⁵⁴ This observation definitely excludes explanation (iii). We assume that the main contribution to the line width stems from inhomogeneity presumably related to the

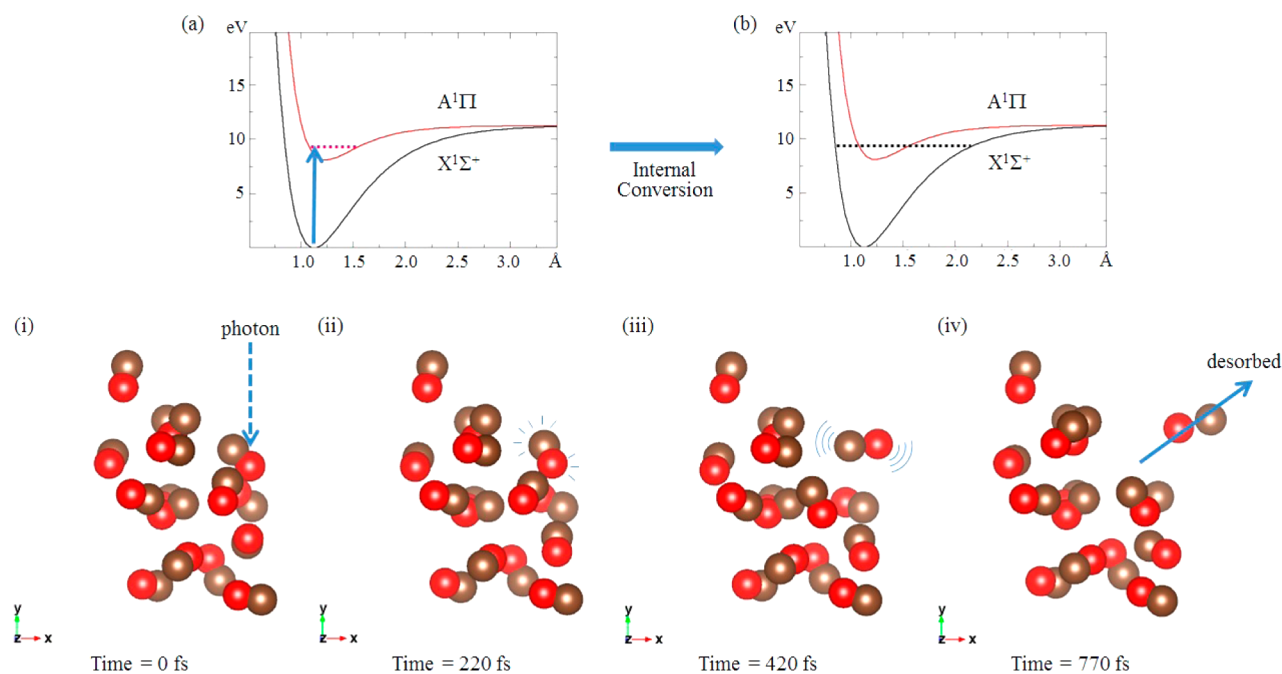


Figure 6. Upper panels: (a) A CO molecule is excited from the X ¹Σ⁺ ground state into the A ¹Π state by absorption of a 9.1 eV photon. The vibration corresponds to that of the v' = 5 level. (b) The molecule has returned to the X ¹Σ⁺ ground state by internal conversion. The vibration corresponds to that of the v' = 48 level. Lower panels: Snap shots of a prototypical photodesorption event. Only the (to be) excited molecule and its 15 nearest neighbors out of a run for 800 molecules at 6 K and 9.1 eV photon energy are shown. From left to right: (i) The conformation after reequilibration, just before the excitation of the indicated molecule. (ii) After 220 fs movement on the excited-state potential, just before return to the ground state. Reorientation of the excited molecule as well as of some of its neighbors is observed. (iii) After 200 fs on the ground-state potential, the originally excited molecule leaves the surface, rotating and with large amplitude vibration. (iv) After 550 fs on the ground-state potential, the surface of the remaining cluster is undergoing reconstruction.

orientational disorder that we find in our MD simulations. Apart from that, we assume that also lifetime broadening plays a role to such an extent (e.g., $\sim 5 \text{ cm}^{-1}$ corresponding to a lifetime of 500 fs) that possibly individual transitions can no longer be distinguished. The decay in this mechanism is due to the coupling of the excited-state vibration with the ground-state rovibrational manifold of the surrounding molecular solid, because expected radiative lifetimes are much longer (expectations are based on gas-phase values that are slightly less than 10 ns for all relevant excited vibrational levels³⁷). We have, therefore, chosen to adopt the mechanism of radiationless de-excitation or internal conversion in our MD simulations. The effects of orientational disorder automatically appear, because we excite every molecule in a sample cluster at an arbitrary moment.

For the amorphous CO clusters, we found no bias for desorption of molecules on the assumed time spent in the excited state, for values between 100 and 500 fs. For the crystalline CO clusters, we did, however, find such a bias, where only molecules that spent close to the maximum time of 500 fs are desorbed. For the crystalline CO clusters, we therefore doubled the excited lifetimes and then a bias was no longer observed. This clearly demonstrates that our model needs this finite excited-state lifetime to adapt to the new force field for the excited CO molecule. This adaptation takes longer for crystalline systems, which is probably caused by the much more rigid structure of the surface layer. Furthermore, it should be mentioned that desorption is never observed when the excitation is simulated to be immediately into a very high vibrational level of the electronic ground state (e.g., v'' ~ 40 for a UV photon of $\sim 8.5 \text{ eV}$), corresponding to an ultrashort

excited-state lifetime. Also desorption is not observed during the time that the molecule spends in the excited state.

After the internal conversion, all the excitation energy appears as vibrational energy of the molecule in the electronic ground state. This vibrational energy largely remains in the excited molecule itself or a neighbor molecule. It is not the vibrational energy itself that causes desorption. In short, there is hardly any vibrational energy transfer on the time scales of our MD simulations after the internal conversion, 5 ps. The mechanism behind the desorption is the landing of the excited molecule onto the ground-state potential energy surface with an unfavorable orientation and position with respect to the surrounding molecules. The binding energy of a regular surface molecule is typically on the order of $\sim 250 \text{ cm}^{-1}$. The difference in the interaction energy for the ground state and the excited state should be enough to break the bond between the surface molecule and the remainder of the cluster. From the contour plots shown in Figures 2–4, one can see that this can easily happen.

From the molecular coordinates and momenta at the end of each of the 5 ps MD trajectory after the internal conversion, the fate of the excited molecule was determined. When a CO molecule was more than 6 Bohr removed from the surface layer of the sample clusters and its binding energy to the remaining cluster was less than its translational energy, we defined it as a desorbed molecule. The illustration of the photodesorption mechanism with snap shots of a prototypical photodesorption event is shown in Figure 6.

We find that the direct desorption mechanism predominantly occurs for the molecules in the top layers of the CO clusters. We also find that the molecules excited in the next top layers

predominantly contribute to desorption through the “kick-out” mechanism by which a neighbor molecule in the top layers desorbs. Moreover, we find that desorption from the inner layers of the clusters is almost negligible. Therefore, we split the CO clusters into the three shells, the core, subsurface, and surface shells, to make an analysis of the desorption probabilities for the respective shells. Our adopted layer width is 3.5 Å, which is consistent with the width between the peaks in the radial distribution functions shown in Figure 5. A summary of the radii used in our classification of core, subsurface, and surface shells of the sample clusters (amorphous CO clusters with 200, 300, 500, 800, and 1200 molecules and crystalline CO clusters containing 221, 522, and 1055 molecules) is given in Table 3.

Table 3. Summary of the Radii Used in Our Classification of Core, Subsurface, and Surface Shells of the Sample Clusters

cluster-type	no. of CO molecules in cluster	shell radius (Å)		
		core	subsurface	surface
amorphous	200	7.0	10.5	14.0
	300	9.0	12.5	16.0
	500	11.0	14.5	18.0
	800	14.0	17.5	21.0
	1200	17.5	21.0	24.5
crystalline	221	6.0	9.5	13.0
	522	10.5	14.0	17.5
	1055	16.0	19.5	23.0

We also analyzed the rotational energy distribution of the desorbed molecules. The average rotational energy is about 0.5 eV with a spread from 0 to 1 eV. The rotational energy is correlated neither with the translational energy nor with the ejection angle. The amount of rotational energy just depends on the local structure around the desorbed molecule.

3.3. Photodesorption probabilities for amorphous CO clusters. In Table 4, we show the summary of the results of our MD simulations for the amorphous CO clusters at 6 K. For each MD trajectory, a selected CO molecule in the core, subsurface, or surface shell of the cluster was excited. We have 5 different samples for each size of the amorphous CO cluster as described in section 2.5. For the 200 molecule samples, we excited every CO molecule. For the 300 and 500 molecule samples, we excited every second molecule. For the 800 molecule samples, we excited only every fifth molecule. For the 1200 molecule samples, we excited every fifth molecule in the surface and subsurface shells but did not excite molecules in the core–shell. The exclusion of the core–shell for the 1200 molecule samples can be justified by the results for the 800 molecule samples where already very little desorption from the core–shell has been observed. The total numbers of MD trajectories summed over the shells are 1000, 750, 1250, 800, and 1200 for the amorphous CO clusters with 200, 300, 500, 800, and 1200 molecules, respectively.

The MD trajectories are classified by the shell to which the selected CO molecule belongs as shown in Table 4. Numbers in parentheses in Table 4 indicate the number of desorption cases by the “kick-out” mechanism, where the excited CO stays in the cluster but a neighbor CO is desorbed. Otherwise, desorption by the direct mechanism occurs, where the excited CO molecule itself is released from the cluster (section 3.2). For the surface shell, we find that about 10% of desorption cases are those by the “kick-out” mechanism. On the contrary,

Table 4. Summary of the Results of MD Simulations for the Amorphous CO Clusters at 6 K

no. of CO molecules in cluster	shell	no. of trajectories for selected CO ^a	no. of trajectories for desorbed CO ^b		
			8.7 eV	9.1 eV	9.5 eV
200	core	150	0	6	2
	subsurface	385	30 (21)	31 (21)	33 (19)
	surface	465	56 (8)	66 (8)	64 (8)
300	core	165	2	3	4
	subsurface	282	11 (9)	17 (13)	13 (12)
	surface	303	32 (4)	37 (2)	31 (3)
500	core	313	1	3	3
	subsurface	397	10 (8)	9 (8)	10 (8)
	surface	540	44 (8)	57 (8)	53 (4)
800	core	257	0	1	0
	subsurface	242	4 (4)	9 (7)	6 (5)
	surface	301	25 (6)	29 (7)	32 (6)
1200	core	609	0	0	0
	subsurface	242	9 (7)	6 (5)	6 (5)
	surface	349	25 (3)	33 (6)	41 (5)

^aFor the 200 molecule samples, we excited individually each CO molecule. For the 300 and 500 molecule samples, we excited every second molecule. For the 800 molecule samples, we excited only every fifth molecule. For the 1200 molecule samples, we excited every fifth molecule in the surface and subsurface shells but did not excite molecules in the core–shell. ^bNumbers in parentheses indicate the number of the desorption cases by the “kick-out” mechanism.

for the subsurface shell, about 90% are desorption cases where a neighbor CO in the surface shell is kicked out. The distance between the excited CO and a desorbing neighbor CO is generally close to 4 Å. Occasionally, we observed that an excited CO and a neighbor CO desorbed simultaneously.

The wavelength dependence of desorption is studied by adapting the excitation energies, 8.7, 9.1, and 9.5 eV, and results are also shown in Table 4. We find that the values for numbers of desorbed CO molecules per shell vary little for the excitation energies 8.7–9.5 eV.

The photodesorption probability per absorbed photon is defined as the number of desorbed molecules after excitation divided by the number of excited molecules in a particular shell. We find that the photodesorption probabilities averaged over the excitation energies of 8.7–9.5 eV are 13.3, 11.0, 9.5, 9.5, and 9.5% for the surface shell of the amorphous CO clusters with 200, 300, 500, 800, and 1200 molecules, respectively. On the contrary, the photodesorption probabilities are 8.1, 4.8, 2.4, 2.6, and 2.9% for the subsurface shell (Table 7). We see that there is a clear trend of decreasing photodesorption probability with increasing sample size. Such a trend is clearly correlated with the increase in the binding energies of both subsurface and surface molecules with increasing sample size (Table 2).

3.4. Photodesorption Probabilities for Crystalline CO Clusters. In Table 5, we present the summary of the results of our MD simulations for the crystalline CO clusters at 6 K. For each MD trajectory, a selected CO molecule in the core, subsurface, or surface shell of the cluster was excited. We made only one sample for each size of the crystalline CO cluster, and thus the statistics is poorer than that for the amorphous CO cluster. Nevertheless, important conclusions can be drawn from the data. For the 221 and 522 molecule samples, we excited

Table 5. Summary of the Results of MD Simulations for the Crystalline CO Clusters at 6 K

no. of CO molecules in cluster	shell	no. of trajectories for selected CO ^a	no. of trajectories for desorbed CO ^b		
			8.7 eV	9.1 eV	9.5 eV
221	core	14	0	0	0
	subsurface	78	1 (1)	0 (0)	1 (1)
	surface	129	3 (0)	8 (0)	10 (1)
522	core	126	0	0	0
	subsurface	123	0 (0)	0 (0)	1 (1)
	surface	273	8 (0)	11 (1)	4 (0)
1055	core	381	0	0	0
	subsurface	302	0 (0)	0 (0)	1 (1)
	surface	372	7 (1)	10 (1)	10 (1)

^aFor the 221 and 522 molecule samples, we excited every CO molecule. For the 1055 molecule sample, we excited every CO molecule in the surface and subsurface shells but did not excite molecules in the core–shell. ^bNumbers in parentheses indicate the number of the desorption cases by the “kick-out” mechanism.

every CO molecule. For the 1055 molecule sample, we excited every molecule in the surface and subsurface shells but did not excite molecules in the core–shell. The exclusion of the core–shell for the 1055 molecule sample can be justified by the results for the smaller samples where no desorption from the core–shell has been observed. The total numbers of MD trajectories summed over the shells are 221, 522, and 674 for

the crystalline CO clusters with 221, 522, and 1055 molecules, respectively.

For the crystalline CO cluster with 221 molecules, we find that the photodesorption probabilities averaged over the excitation energies of 8.7–9.5 eV is 5.4% for the surface shell and 0.9% for the subsurface shell. For the surface shell the observed desorption cases are predominantly those by the direct mechanism where the excited CO itself is desorbed, whereas for the subsurface shell the only desorption cases observed are where a neighbor CO in the surface shell is kicked out. There is no desorption from the core–shell. For the crystalline CO clusters with 522 and 1055 molecules, the photodesorption probabilities averaged over the excitation energies of 8.7–9.5 eV are, respectively, 2.8% and 2.3% for the surface shell and are an order of magnitude smaller for the subsurface shell (Table 7). We can see that for larger crystalline CO clusters the photodesorption probabilities decrease even further, especially when compared with values for amorphous ice. We interpret this decrease as a demonstration of the increasing binding energy of surface molecules with increasing cluster size (Table 2).

Furthermore, we can see that the photodesorption probabilities for larger crystalline CO clusters are 5 times smaller than those for the amorphous CO clusters. Clearly, the much more regular structure of the crystalline clusters leads to stronger binding of surface molecules and a lower photodesorption probability.

3.5. Temperature Dependence of Photodesorption Probabilities. In Table 6, we summarize the results of MD

Table 6. Summary of the Results of MD Simulations To Study the Temperature Dependence of the Photodesorption Probabilities per Absorbed UV Photon for the Amorphous CO Clusters with 800 and 1200 Molecules

no. of CO molecules in cluster	shell	no. of trajectories for selected CO ^a	temp of cluster (K)	no. of trajectories for desorbed CO ^b		
				8.7 eV	9.1 eV	9.5 eV
800	core	257	6	0	1	0
			12	1	2	2
			18	0	1	2
			24	0	1	1
	subsurface	242	6	4 (4)	9 (7)	6 (5)
			12	8 (7)	6 (4)	4 (4)
			18	9 (8)	10 (9)	7 (6)
			24	14 (11)	11 (10)	13 (13)
	surface	301	6	25 (6)	29 (7)	32 (6)
			12	23 (6)	28 (4)	34 (4)
			18	24 (2)	32 (9)	27 (5)
			24	22 (1)	28 (4)	42 (7)
1200	core	304	6	0	0	0
			12	0	0	0
			18	0	0	0
			24	0	0	0
	subsurface	121	6	3 (3)	4 (4)	2 (2)
			12	3 (2)	7 (6)	3 (2)
			18	4 (2)	5 (3)	4 (3)
			24	4 (3)	7 (6)	5 (4)
	surface	175	6	15 (1)	14 (1)	14 (1)
			12	21 (0)	13 (0)	22 (0)
			18	17 (2)	13 (2)	25 (0)
			24	23 (3)	24 (5)	26 (0)

^aFor the 800 molecule samples, we excited every fifth CO molecule. For the 1200 molecule samples, we excited every 10th molecule in the surface and subsurface shells but did not excite molecules in the core–shell. ^bNumbers in parentheses indicate the number of the desorption cases by the “kick-out” mechanism.

Table 7. Summary of the Photodesorption Probabilities per Absorbed UV Photon

cluster-type	no. of CO molecules in cluster	photodesorption probability (%) ^a							
		surface				subsurface			
		6 K	12 K	18 K	24 K	6 K	12 K	18 K	24 K
amorphous	200	13.3				8.1			
	300	11.0				4.8			
	500	9.5				2.4			
	800	9.5	9.4	9.2	10.2	2.6	2.5	3.6	5.2
	1200	9.5	10.7	10.5	13.4	2.9	3.6	3.6	4.4
crystalline	221	5.4				0.9			
	522	2.8				0.3			
	1055	2.3				0.2			

^aPhotodesorption probability is defined as the number of desorbed molecules after excitation divided by the number of excited molecules in a particular shell. The values averaged over the excitation energies of 8.7–9.5 eV are shown here for the surface and subsurface shell at a particular cluster temperature.

simulations to study the temperature dependence of the photodesorption probabilities for the amorphous CO clusters with 800 and 1200 molecules. Here, the effect of the temperature of CO clusters was examined by raising the temperature in the re-equilibration phase to 12, 18, or 24 K instead of 6 K. For each MD trajectory, a selected CO molecule in the core, subsurface, or surface shell of the cluster was excited. We have five different samples for each size of the amorphous CO cluster. For the 800 molecule samples, we excited every fifth CO molecule. For the 1200 molecule samples, we excited every 10th molecule in the surface and subsurface shells but did not excite molecules in the core–shell. The total numbers of MD trajectories for which the effect of the temperature of CO clusters was examined are 800 and 600 for the amorphous CO clusters with 800 and 1200 molecules, respectively.

For the amorphous CO clusters with 800 molecules, we find that the photodesorption probabilities for the surface shell are nearly constant around 9.5% with excitation energies of 8.7–9.5 eV at cluster temperatures of 6–18 K. On the contrary, the photodesorption probabilities for the surface shell are 14% with 9.5 eV at 24 K. The photodesorption probabilities for the subsurface shell are around 2.5% with 8.7–9.5 eV at 6 and 12 K. There is an increase in the photodesorption probabilities for the subsurface shell at 18 and 24 K. We can see that both higher excitation energy and higher cluster temperature give a boost in the photodesorption probabilities. Clearly, the combined effect of large amplitude motions of the molecules and softening of the cluster surface plays a role.

For the amorphous CO clusters with 1200 molecules, the statistics are rather poor, because only every 10th molecule in each sample cluster was excited. There is little effect of increased temperature up to 18 K. The photodesorption probabilities for the surface shell are 9.5, 10.7, and 10.5% at 6, 12, and 18 K, respectively, and the values of the photodesorption probabilities for the subsurface shell are about one-third of those for the surface shell. Only at 24 K is there about a 30% increase in the photodesorption probabilities, for both the surface shell and the subsurface shell.

In Table 7, values of the photodesorption probabilities averaged over the excitation energies of 8.7–9.5 eV for the surface and subsurface shell at a particular cluster temperature are shown as the main results of our simulations. For larger amorphous CO clusters, the photodesorption probability for the surface shell approaches a value around 9.5% and that for the subsurface shell approaches a value around 3% at

temperatures below 18 K, whereas those values increase above 24 K. For larger crystalline clusters, the photodesorption probability for the surface shell approaches a value around 2% and desorption from the subsurface shell is negligible.

3.6. Comparison with Experiments. In the experiments by Öberg et al.,^{17–19} it was shown that photodesorption of CO ice arises only from the top few layers, shown by the independence on layer thickness and confirmed in experiments with intermittent layers of C¹⁸O or N₂. Their results were confirmed by the more recent experiments by Muñoz Caro et al.,²⁰ Fayolle et al.,²¹ and Bertin et al.⁵⁸ We find in our simulations that photodesorption by the direct desorption mechanism where the excited CO molecule itself is released only occurs from the top layers, whereas photodesorption by the “kick-out” desorption mechanism where the excited CO molecule stays in the cluster but kicks out a neighboring CO molecule can occur in the next layers below the top. These findings are in accord with the conclusions from the experiments, where not just CO but also a neighboring N₂ molecule can be desorbed. Clearly, only a tiny fraction of the photon energy is transferred into translational motion of the absorbing molecule.

The calculated binding energy of molecules in the surface layers of amorphous CO clusters is ~250 cm⁻¹ compared to 500–650 cm⁻¹ for the layers below (the binding energy of molecules in the surface layer of crystalline clusters is larger than 400 cm⁻¹). In our proposed mechanism, this 250 cm⁻¹ is overcome by the change in the interaction energy when the excited molecule, after it has had time to find a “favorable” position and orientation with respect to its neighboring molecules, undergoes radiationless decay to the ground state where now the orientation and position may be unfavorable. This mechanism is an extension of the mechanism for photodesorption of CO ice proposed in earlier experimental papers.¹⁷ The immediate decay of the excited-state vibrational level into a ground-state vibrational level did not lead to desorption in our simulations. The finding of a new position and orientation on the ground-state potential energy surface by the molecule that spends a finite time in the excited state is essential. We have followed this process by tracing the energy of the CO molecules during MD trajectories.

Desorption by the direct mechanism leads to molecules that are still very hot vibrationally. Only a fraction of the photon energy is lost to the lattice or transferred into rotation and translation. On the contrary, the molecules desorbed by the “kick-out” mechanism have only little energy in vibration,

rotation, and translation. Thus, experimentalists should be able to observe a bimodal vibrational distribution of the desorbed molecules. In astrophysical situations, the product distribution is less relevant, because the molecule will undergo radiative decay on ms time scales, much shorter than times between collisions.

We can also compare our results with the recent experiments by Fayolle et al.²¹ They used a tunable VUV light source for the first time in experimental photodesorption. They verified that the photodesorption probability per incident photon (the number of desorbed CO molecules detected in a QMS) was proportional to the wavelength dependent VUV radiation absorbance as determined by Lu et al.⁵⁴ for a thin layer of frozen CO at 10 K. This implies that according to the experiments there is no effect of the excitation energy on the photodesorption probability.

Our results are in accord with the observed independence of wavelength for the 9.1–9.5 eV range, but not completely for 8.7 eV. Possibly this is on the low energy side due to the fact that our vibrational amplitudes are limited to the classical range of the CO potentials. Indeed, our photodesorption probabilities by the “kick-out” mechanism are generally relatively low at 8.7 eV, implying a less effective “kick-out” mechanism that might be related to the vibrational amplitude. These amplitudes are small anyway at 8.7 eV.

Our predicted slight increase in the photodesorption probability with increasing cluster temperature is not consistent with the observed decrease in the experiments. This is likely related to the fact that the MD simulations span only picoseconds, whereas the experiments are done on a time scale of hours, so direct comparison is difficult. Presumably, the rise of temperature causes a slight loss of order in the amorphous CO crystal in the experiments. From our simulations of crystalline CO clusters, we know that the photodesorption probability is reduced by around a factor of 5 compared to that for the amorphous CO clusters. Suggestions to the experimentalists would be to do a hysteresis experiment to determine the photodesorption rate as a function of temperature, by increasing stepwise from 10 to 25 K starting from a sample freshly prepared at 10 K and once going back from 25 to 10 K. If sample order is introduced in this way, it will show up as a difference in the photodesorption probability at 10 K between initial and final sample.

The main astrophysical interest is in the photodesorption probability per incident photon rather than per absorbed photon. To convert our probabilities to these units, we need to know the photon absorption cross section of solid CO. Only very recently has the photon absorption cross section of solid CO been determined experimentally with presumably sufficient accuracy in the layer thickness determination by Cruz-Diaz et al.²³ The experimental absorption cross section at 8.2 eV is given as $15 \times 10^{-18} \text{ cm}^2$ with an uncertainty of $\pm 8\%$. The most recent experimental value for the photodesorption probability is given by Fayolle et al.²¹ as $(2.8 \pm 1.7) \times 10^{-2}$ molecules photon^{-1} at the corresponding peak maximum of 8.2 eV in the solid CO absorption spectrum for excitation into the $v' = 1$ level of the $A^1\Pi$ state at 18 K.

From the density of our CO cluster of 1.05 g cm^{-3} we derive a density of 22.6×10^{21} molecules cm^{-3} . In a layer with a thickness of $\sim 3.5 \text{ \AA}$ the absorbance would thus be $15 \times 10^{-18} \times 22.6 \times 10^{21} \times 3.5 \times 10^{-8} = 0.0119$, implying that only $\sim 3\%$ of the photons (1 out of 35 photons) would be absorbed in that layer. From Table 7, we get photodesorption probabilities of

9.5% and 3% per absorbed photon, respectively, for the surface shell and the subsurface shell for larger amorphous CO clusters at temperatures below 18 K. We thus take this photodesorption probability of 12.5% as the value including all desorption from the top layer either by the direct desorption mechanism (the excited molecule in the surface shell itself is desorbed) or by the “kick-out” one (the excited molecule in the subsurface shell kicks out a neighbor molecule in the surface shell). Then, our predicted photodesorption probability per incident photon would be $0.03 \times 0.125 = 4.0 \times 10^{-3}$ molecules photon^{-1} .

Our predicted value of the photodesorption rate is 3–11 times smaller than that given in the experiments by Fayolle et al.²¹ Their higher values combined with the new value for the absorption cross section would imply that every photon absorbed in the surface layer would lead to desorption of a CO molecule. We speculate on the origin of the discrepancy as follows;

- (1) Our simulation time after the internal conversion is only 5 ps, which might be too short. On a longer time scale in laboratory experiments, the photon energy will be further transferred into large amplitude molecular vibrations leading ultimately to desorption. After photon absorption, some molecules drift from one layer to the upper one and are then bound by much less than the average energy (typically by $100\text{--}200 \text{ cm}^{-1}$ only). If the ice flake is hit by a next photon shortly afterward, release of surface molecules is much easier. In the laboratory experiments, this situation could arise, because the photon intensity is huge, at least 6 orders of magnitude larger than in dense clouds.
- (2) The experimental photodesorption probability derived by Fayolle et al.²¹ may have larger uncertainties, possibly because the rate depends strongly on the assumed value of the photon flux and its dependence with wavelength. Presumably, this is already accounted for in the large uncertainties in the given value.
- (3) The experimental temperature assumed by Fayolle et al.,²¹ 18 K, the lowest value that could be reached in their setup, may be an underestimate. Their results may have been for a higher ice temperature. The exact temperature of the ice is in particular relevant because Muñoz Caro et al.²⁰ observed thermal desorption of CO already at 15 K in their very well temperature controlled experiments. In our simulations, cluster temperatures above 18 K give an increase in the photodesorption probabilities.

4. CONCLUSIONS

The photodesorption process of CO ice is successfully reproduced by our classical MD simulations, where we calculated *ab initio* 4-dimensional potential energy surfaces and developed the site–site potential energy functions for the ground and excited-state nonrigid CO dimer, because the vibrational motions and the electronic excited states play important roles for the photodesorption process.

At the first stage of our simulations, we generated two types of CO clusters, amorphous and crystalline ones, as models of pieces of interstellar CO ice. We examined the radial distribution functions, the densities, the lattice energies, and the specific heats of these clusters, and find that there are clear differences in these properties between amorphous and crystalline CO clusters.

At the second stage of our simulations, we brought a selected CO molecule into the excited state vertically by an energy corresponding to a UV photon. After a finite lifetime on the excited-state potential energy surface, we brought back the CO molecule into the ground state vertically. The landing of the excited molecule onto the ground-state potential energy surface with an unfavorable orientation and position with respect to the surrounding molecules is essential for the CO molecule to be desorbed from the cluster.

It is found that there are two desorption mechanisms: (1) the direct desorption mechanism where the excited CO molecule itself is released from the cluster, which predominantly occurs for the molecules in the surface shell; (2) the “kick-out” desorption mechanism where the excited CO molecule stays in the cluster but kicks out a neighbor CO molecule, which predominantly occurs in the subsurface shell and kicks out a neighbor molecule in the surface shell. It is found that about 10% and 90% of desorption cases are those by the “kick-out” mechanism for the surface and subsurface shell, respectively. It is also found that there are almost no desorption cases for the molecules in the core shell. These findings are in accord with the conclusions from the laboratory experiments.

We examined the effects of the cluster size (200–1200 molecules for amorphous CO clusters and 221–1055 molecules for crystalline CO clusters), the excitation energy (8.7–9.5 eV), and the cluster temperature (6–24 K). The photodesorption probabilities decrease significantly for larger clusters. This trend should be correlated with the increase in the binding energies of the molecules in the surface and subsurface shells with increasing cluster size. The effect of the excitation energy is very small for the energy range 8.7–9.5 eV. The effect of an increase in the cluster temperature is small for temperatures below 18 K, but there is some increase in the photodesorption probability above 18 K. Both higher excitation energy and higher cluster temperature give an increase in the photodesorption probabilities. This suggests the combined effect of large amplitude motions of the molecules and softening of the cluster surface.

The photodesorption probability per absorbed UV photon is defined as the number of desorbed molecules after excitation divided by the number of excited molecules in a particular shell. In Table 7, values of the photodesorption probabilities averaged over the excitation energies of 8.7–9.5 eV for the surface and subsurface shell at a particular cluster temperature are summarized as the main results of our simulations. For larger amorphous CO clusters, the photodesorption probability for the surface shell approaches a value around 9.5% and that for the subsurface shell approaches a value around 3% at temperatures below 18 K. For larger crystalline clusters, the photodesorption probability for the surface shell approaches a value around 2% and desorption from the subsurface shell is negligible.

The photodesorption probabilities per absorbed photon for the crystalline CO clusters are 5 times smaller than those for the amorphous CO clusters. Clearly, the much more regular structure of the crystalline clusters leads to stronger binding of surface molecules and a lower photodesorption probability.

Our predicted photodesorption probability per incident UV photon is 4.0×10^{-3} molecules photon⁻¹. This value is a factor of 3–11 smaller than that given in the experiments by Fayolle et al.²¹ at 8.2 eV. The origin of the discrepancy is speculated as the limited time scale in our MD simulations, higher photon intensity in the laboratory experiments leading to absorption of

a second photon before the surface has relaxed: the molecule is gone, the surface remains behind in a “damaged” state where the binding for molecules close to the “leaved behind gap” has become weaker.

Astrochemical models demonstrate that inclusion of UV photodesorption with yields comparable to those computed here can indeed significantly increase the abundance of gas-phase CO in cold clouds and improve comparison with observations.⁵⁹ For example, Walsh et al.⁶⁰ show in their Figure 8 that the gas-phase CO abundance is enhanced by several orders of magnitude in the midplane of protoplanetary disks when CO photodesorption is taken into account.

AUTHOR INFORMATION

Corresponding Author

*M. C. van Hemert. E-mail: m.hemert@chem.leidenuniv.nl.

Notes

The authors declare no competing financial interest.

ACKNOWLEDGMENTS

We are grateful to Dr. K. I. Öberg, Dr. E. Fayolle, Prof. H. Linnartz, and the members of the astrochemistry group in Leiden University for useful discussions, and support from Meiji Gakuin University for 12 months visit to Leiden where this work was initiated. Astrochemistry in Leiden is supported by The Netherlands Research School for Astronomy (NOVA), and by a Spinoza award and the Dutch Astrochemistry Network financed by The Netherlands Organization for Scientific Research (NWO). The cluster computer facilities of the Leiden Theory group, where most of the computations were performed, were also financed through a TOP grant from NWO Chemical Sciences. A part of preliminary computations were performed using Research Center for Computational Science, Okazaki, Japan.

REFERENCES

- (1) Tielens, A. G. G. M.; Charnley, S. B. *Origins Life Evol. Biospheres* **1997**, *27*, 23–51.
- (2) Cuppen, H. M.; van Dishoeck, E. F.; Herbst, E.; Tielens, A. G. G. M. Microscopic Simulation of Methanol and Formaldehyde Ice Formation in Cold Dense Cores. *Astron. Astrophys.* **2009**, *508*, 275–287.
- (3) Herbst, E.; van Dishoeck, E. F. Complex Organic Interstellar Molecules. *Annu. Rev. Astron. Astrophys.* **2009**, *47*, 427–480.
- (4) Gibb, E. L.; Whittet, D. C. B.; Boogert, A. C. A.; Tielens, A. G. G. M. Interstellar Ice: The Infrared Space Observatory Legacy. *Astrophys. J., Suppl. Ser.* **2004**, *151*, 35–73.
- (5) Öberg, K. I.; Boogert, A. C. A.; Pontoppidan, K. M.; van den Broek, S.; van Dishoeck, E. F.; Bottinelli, S.; Blake, G. A.; Evans, N. J., II The Spitzer Ice Legacy: Ice Evolution from Cores to Protostars. *Astrophys. J.* **2011**, *740*, 109.
- (6) Millar, T. J.; Williams, D. A. Dust and Astrochemistry: an Introduction. In *Dust and Chemistry in Astronomy*; Millar, T. J., Williams, D. A., Eds.; Institute of Physics Publishing: London, 1993; pp 1–8.
- (7) Whittet, D. C. B. *Dust in the Galactic Environment*, 2nd ed.; CRC Press: London, 2002.
- (8) Tielens, A. G. G. M.; Tokunaga, A. T.; Geballe, T. R.; Baas, F. Interstellar Solid CO - Polar and Nonpolar Interstellar Ices. *Astrophys. J.* **1991**, *381*, 181–199.
- (9) Boogert, A. C. A.; Hogerheijde, M. R.; Blake, G. A. High-Resolution 4.7 micron Keck/NIRSPEC Spectra of Protostars. I. Ices and Infalling Gas in the Disk of L1489 IRS. *Astrophys. J.* **2002**, *568*, 761–770.

- (10) Pontoppidan, K. M.; Fraser, H. J.; Dartois, E.; Thi, W.-F.; van Dishoeck, E. F.; Boogert, A. C. A.; d'Hendecourt, L.; Tielens, A. G. G. M.; Bisschop, S. E. A 3–5 μm VLT Spectroscopic Survey of Embedded Young Low Mass Stars I. Structure of the CO Ice. *Astron. Astrophys.* **2003**, *408*, 981–1007.
- (11) Bergin, E. A.; Alves, J.; Huard, T.; Lada, C. J. N_2H^+ and C^{18}O Depletion in a Cold Dark Cloud. *Astron. Astrophys. J.* **2002**, *570*, L101–L104.
- (12) Dartois, E.; Dutrey, A.; Guilloteau, S. Structure of the DM Tau Outer Disk: Probing the Vertical Kinetic Temperature Gradient. *Astron. Astrophys.* **2003**, *399*, 773–787.
- (13) Piétu, V.; Dutrey, A.; Guilloteau, S. Probing the Structure of Protoplanetary Disks: a Comparative Study of DM Tau, LkCa 15, and MWC 480. *Astron. Astrophys.* **2007**, *467*, 163–178.
- (14) Prasad, S. S.; Tarafdar, S. P. UV Radiation Field Inside Dense Clouds – Its Possible Existence and Chemical Implications. *Astron. Astrophys. J.* **1983**, *267*, 603–609.
- (15) Willacy, K.; Langer, W. D. The Importance of Photoprocessing in Protoplanetary Disks. *Astron. Astrophys. J.* **2000**, *544*, 903–920.
- (16) Dominik, C.; Ceccarelli, C.; Hollenbach, D.; Kaufman, M. Gas-Phase Water in the Surface Layer of Protoplanetary Disks. *Astron. Astrophys. J.* **2005**, *635*, L85–L88.
- (17) Öberg, K. I.; Fuchs, G. W.; Awad, Z.; Fraser, H. J.; Schlemmer, S.; van Dishoeck, E. F.; Linnartz, H. Photodesorption of CO Ice. *Astron. Astrophys. J.* **2007**, *662*, L23–L26.
- (18) Öberg, K. I.; van Dishoeck, E. F.; Linnartz, H. Photodesorption of Ices I: CO, N_2 , and CO_2 . *Astron. Astrophys.* **2009**, *496*, 281–293.
- (19) Öberg, K. I.; Linnartz, H.; Visser, R.; van Dishoeck, E. F. Photodesorption of Ices. II. H_2O and D_2O . *Astron. Astrophys. J.* **2009**, *693*, 1209–1218.
- (20) Muñoz Caro, G. M.; Jiménez-Escobar, A.; Martín-Gago, J. Á.; Rogero, C.; Atienza, C.; Puertas, S.; Sobrado, J. M.; Torres-Redondo, J. New Results on Thermal and Photodesorption of CO Ice Using the Novel InterStellar Astrochemistry Chamber (ISAC). *Astron. Astrophys.* **2010**, *522*, A108.
- (21) Fayolle, E. C.; Bertin, M.; Romanzin, C.; Michaut, X.; Öberg, K. I.; Linnartz, H.; Fillion, J.-H. CO Ice Photodesorption: A Wavelength-Dependent Study. *Astron. Astrophys. J., Lett.* **2011**, *739*, L36.
- (22) Chen, Y.-J.; Chuang, K.-J.; Muñoz Caro, G. M.; Nuevo, M.; Chu, C.-C.; Yih, T.-S.; Ip, W.-H.; Wu, C.-Y. R. Vacuum Ultraviolet Emission Spectrum Measurement of a Microwave-Discharge Hydrogen-Flow Lamp in Several Configurations: Application to Photodesorption of CO Ice. *Astron. Astrophys. J.* **2014**, *781*, 15.
- (23) Cruz-Díaz, G. A.; Muñoz Caro, G. M.; Chen, Y.-J.; Yih, T.-S. Vacuum-UV Spectroscopy of Interstellar Ice Analogs. I. Absorption Cross-Sections of Polar-Ice Molecules. *Astron. Astrophys.* **2014**, *562*, A119.
- (24) Greenberg, J. M. Some Scattering Problems of Interstellar Grains, In *Interstellar Dust and Related Topics* (IAU Symp. 52); Greenberg, J. M., van de Hulst, H. C., Eds.; Springer: Dordrecht, 1973; pp 3–9.
- (25) Fuchs, G. W.; Acharyya, K.; Bisschop, S. E.; Öberg, K. I.; van Broekhuizen, F. A.; Fraser, H. J.; Schlemmer, S.; van Dishoeck, E. F.; Linnartz, H. Comparative Studies of O_2 and N_2 in Pure, Mixed and Layered CO Ices. *Faraday Discuss.* **2006**, *133*, 331.
- (26) Andersson, S.; Al-Halabi, A.; Kroes, G.-J.; van Dishoeck, E. F. Molecular-Dynamics Study of Photodissociation of Water in Crystalline and Amorphous Ices. *J. Chem. Phys.* **2006**, *124*, 064715.
- (27) Andersson, S.; van Dishoeck, E. F. Photodesorption of Water Ice. A Molecular Dynamics Study. *Astron. Astrophys.* **2008**, *491*, 907–916.
- (28) Arasa, C.; Andersson, S.; Cuppen, H. M.; van Dishoeck, E. F.; Kroes, G.-J. Molecular Dynamics Simulations of the Ice Temperature Dependence of Water Ice Photodesorption. *J. Chem. Phys.* **2010**, *132*, 184510.
- (29) Galloway, E. T.; Herbst, E. The Desorption of CO from Interstellar Grains. *Astron. Astrophys.* **1994**, *287*, 633–640.
- (30) Dzegilenko, F.; Herbst, E. A New Desorption Mechanism for Condensed Phase Interstellar CO. *Astron. Astrophys. J.* **1995**, *443*, L81–L83.
- (31) Vanden Bout, P. A.; Steed, J. M.; Bernstein, L. S.; Klemperer, W. Laboratory Measurements and a Search for Interstellar CO Dimer. *Astron. Astrophys. J.* **1979**, *234*, 503–505.
- (32) Havenith, M.; Petri, M.; Lubina, C.; Hilpert, G.; Urban, W. IR Spectroscopy of $(\text{CO})_2$ Using Concentration-Frequency Double Modulation in a Supersonic Jet Expansion. *J. Mol. Spectrosc.* **1994**, *167*, 248–261.
- (33) Brookes, M. D.; McKellar, A. R. W. The Mystery of the CO Dimer: Assignments from Variable-Temperature Jet-Cooled Infrared Spectra. *Chem. Phys. Lett.* **1998**, *287*, 365–370.
- (34) van der Pol, A.; van der Avoird, A.; Wormer, P. E. S. An Ab Initio Intermolecular Potential for the Carbon Monoxide Dimer $(\text{CO})_2$. *J. Chem. Phys.* **1990**, *92*, 7498–7504.
- (35) Meredith, A. W.; Stone, A. J. An ab Initio and Diffusion Monte Carlo Study of the Potential Energy Surface of the CO Dimer. *J. Phys. Chem. A* **1998**, *102*, 434–445.
- (36) Vissers, G. W. M.; Wormer, P. E. S.; van der Avoird, A. An Ab Initio CO Dimer Interaction Potential and the Computation of the Rovibrational Spectrum of $(\text{CO})_2$. *Phys. Chem. Chem. Phys.* **2003**, *5*, 4767–4771.
- (37) Dawes, R.; Wang, X.-G.; Carrington, T., Jr. CO Dimer: New Potential Energy Surface and Rovibrational Calculations. *J. Phys. Chem. A* **2013**, *117*, 7612–7630.
- (38) Karssemeijer, L. J.; Ioppolo, S.; van Hemert, M. C.; van der Avoird, A.; Allodi, M. A.; Blake, G. A.; Cuppen, H. M. Dynamics of CO in Amorphous Water-Ice Environments. *Astron. Astrophys. J.* **2014**, *781*, 16.
- (39) Boys, S. F.; Bernardi, F. The Calculation of Small Molecular Interactions by the Differences of Separate Total Energies. Some Procedures with Reduced Errors. *Mol. Phys.* **1970**, *19*, 553–566.
- (40) MOLPRO is a software package used for accurate *ab initio* quantum chemistry calculations, designed and maintained by H.-J. Werner and P. J. Knowles, and containing contributions from a number of other authors.
- (41) Berns, R. M.; van der Avoird, A. N_2 – N_2 Interaction Potential from Ab Initio Calculations, with Application to the Structure of $(\text{N}_2)_2$. *J. Chem. Phys.* **1980**, *72*, 6107–6116.
- (42) van Hemert, M. C. Potential Energy Surface for the Study of Inelastic Collisions between Nonrigid CO and H_2 . *J. Chem. Phys.* **1983**, *78*, 2345–2354.
- (43) Lim, T.-C. Alignment of Buckingham Parameters to Generalized Lennard-Jones Potential Functions. *Z. Naturforsch., A: Phys. Sci.* **2009**, *64*, 200–204.
- (44) Cooper, D. L.; Kirby, K. Theoretical Study of Low-Lying $^1\Sigma^+$ and $^1\Pi$ States of CO. I. Potential Energy Curves and Dipole Moments. *J. Chem. Phys.* **1987**, *87*, 424–432.
- (45) Borges, I., Jr.; Caridade, P. J. S. B.; Varandas, A. J. C. Potential Energy Curves for $X^1\Sigma^+$ and $A^1\Pi$ States of CO: The $A^1\Pi$ ($v'=1-23$) $\leftarrow X^1\Sigma^+$ ($v''=0, 1$) Transitions. *J. Mol. Spectrosc.* **2001**, *209*, 24–29.
- (46) Kaiser, R. I. Experimental Investigation on the Formation of Carbon-Bearing Molecules in the Interstellar Medium via Neutral–Neutral Reactions. *Chem. Rev.* **2002**, *102*, 1309–1358.
- (47) Nelder, J. A.; Mead, R. A Simplex Method for Function Minimization. *Computer J.* **1965**, *7*, 308–313.
- (48) Vegard, L. Struktur und Leuchtfaehigkeit von festem Kohlenoxyd. *Eur. Phys. J. A* **1930**, *61*, 185–190.
- (49) Verlet, L. Computer “Experiments” on Classical Fluids. I. Thermodynamical Properties of Lennard-Jones Molecules. *Phys. Rev.* **1967**, *159*, 98–103; Computer “Experiments” on Classical Fluids. II. Equilibrium Correlation Functions. *Phys. Rev.* **1968**, *165*, 201–214.
- (50) Berendsen, H. J. C.; Postma, J. P. M.; van Gunsteren, W. F.; DiNola, A.; Haak, J. R. Molecular Dynamics with Coupling to an External Bath. *J. Chem. Phys.* **1984**, *81*, 3684–3690.
- (51) Janssen, W. B. J. M.; Michiels, J.; van der Avoird, A. Lattice Dynamics of α -CO from an Ab Initio Potential. *J. Chem. Phys.* **1991**, *94*, 8402–8407.
- (52) Vissers, G. W. M.; Heßelmann, A.; Jansen, G.; Wormer, P. E. S.; van der Avoird, A. New CO–CO Interaction Potential Tested by Rovibrational Calculations. *J. Chem. Phys.* **2005**, *122*, 054306.

(53) Krupskii, I. N.; Prokhvatilov, A. I.; Erenburg, A. I.; Yantsevich, L. D. Structure and Thermal Expansion of α -CO. *Phys. Status Solidi A* **1973**, *19*, 519–527.

(54) Lu, H.-C.; Chen, H.-K.; Cheng, B.-M.; Kuo, Y.-P.; Ogilvie, J. F. Spectra in the Vacuum Ultraviolet Region of CO in Gaseous and Solid Phases and Dispersed in Solid Argon at 10 K. *J. Phys. B: At., Mol. Opt. Phys.* **2005**, *38*, 3693–3704.

(55) Mason, N. J.; Dawes, A.; Holtom, P. D.; Mukerji, R. J.; Davis, M. P.; Sivaraman, B.; Kaiser, R. I.; Hoffmann, S. V.; Shaw, D. A. VUV Spectroscopy and Photo-Processing of Astrochemical Ices: an Experimental Study. *Faraday Discuss.* **2006**, *133*, 311.

(56) Craig, D. P.; Walmsley, S. H. *Excitons in Molecular Crystals*; Benjamin: New York, 1968.

(57) Field, R. W.; Benoist d'Azy, O.; Lavollée, M.; Lopez-Delgado, R.; Tramer, A. Radiative Decay Rates from Deperturbed $v=0-7$ Vibrational Levels of CO A¹Π Measured using Synchrotron Radiation. *J. Chem. Phys.* **1983**, *78*, 2838–2846.

(58) Bertin, M.; Fayolle, E. C.; Romanzin, C.; Poderoso, H. A. M.; Michaut, X.; Philippe, L.; Jeseck, P.; Öberg, K. I.; Linnartz, H.; Fillion, J.-H. Indirect Ultraviolet Photodesorption from CO:N₂ Binary Ices – an Efficient Grain-Gas Process. *Astrophys. J.* **2013**, *779*, 120.

(59) Keto, E.; Caselli, P. Dynamics and Depletion in Thermally Supercritical Starless Cores. *Mon. Not. R. Astron. Soc.* **2010**, *402*, 1625–1634.

(60) Walsh, C.; Millar, T. J.; Nomura, H. Chemical Processes in Protoplanetary Disks. *Astrophys. J.* **2010**, *722*, 1607–1623.